applied sciences

MDPI

Article

Tribological Analysis of Steels in Fuel Environments: Impact of Alloy Content and Hardness

Ali Z. Macknojia [1], Vanessa L. Montoya [1], Euan Cairns [1], Mohammad Eskandari [1], Shuangbiao Liu [2], Yip-Wah Chung [2,3], Q. Jane Wang [2], Stephen P. Berkebile [4], Samir M. Aouadi [1], Andrey A. Voevodin [1] and Diana Berman [1,*]

[1] Materials Science and Engineering Department, University of North Texas, 1155 Union Circle, Denton, TX 76203, USA; samir.aouadi@unt.edu (S.M.A.); andrey.voevodin@unt.edu (A.A.V.)
[2] Department of Mechanical Engineering, Northwestern University, Evanston, IL 60208, USA; shuangbiao.liu@northwestern.edu (S.L.); qwang@northwestern.edu (Q.J.W.)
[3] Department of Materials Science and Engineering, Northwestern University, Evanston, IL 60208, USA
[4] DEVCOM Army Research Laboratory, Aberdeen Proving Ground, Aberdeen, MD 21005, USA
* Correspondence: diana.berman@unt.edu

Abstract: The performance and durability of high-pressure fuel systems in combustion engines are critical for consistent operation under extreme conditions. High-pressure fuel systems are traditionally lubricated with fuel that is compressed and delivered to the combustion chamber. However, lubrication with fuel presents significant challenges in these systems when used with low-viscosity fuels, leading to increased wear rates, especially in reciprocating contacts. This study delved into the tribological performance of steels of varying alloy content (annealed and hardened variants of AISI-52100, CF2, and D2) against alumina and hard 52100 counterbody materials in ethanol and decane environments. Friction and wear behaviors were evaluated, highlighting the influence of material interactions and environmental factors. Elastohydrodynamic lubrication analysis of the tested systems indicated that ethanol and decane form lubricating films of nanometer-scale thickness, confirming the boundary lubrication regimes of the performed tests. In summary, the tribological behavior trends were similar for alumina and 52100 counterbodies. Even though soft 52100 steel demonstrated low friction, its wear was the largest for both tested environments and counterface materials. Among all the tested materials, hard D2 experienced the lowest wear. 52100 and D2 steels showed opposite friction change behavior when comparing hard and soft samples, with lower friction observed for softer 52100 steel and harder D2 steel. Meanwhile, the wear was lower for harder candidates than for softer ones independent of the environment and counterbody material. Raman spectroscopy analysis of the formed wear tracks indicated the formation of carbon films with larger intensities of characteristic carbon peaks observed for more wear-resistant materials. These results suggest the synergistic effect of hardness and tribochemical activity in reducing the wear of materials.

Keywords: friction; ethanol; decane; steel; hardness; lubrication; tribochemistry; elastohydrodynamic lubrication analysis; wear

Citation: Macknojia, A.Z.; Montoya, V.L.; Cairns, E.; Eskandari, M.; Liu, S.; Chung, Y.-W.; Wang, Q.J.; Berkebile, S.P.; Aouadi, S.M.; Voevodin, A.A.; et al. Tribological Analysis of Steels in Fuel Environments: Impact of Alloy Content and Hardness. *Appl. Sci.* **2024**, *14*, 1898. https://doi.org/10.3390/app14051898

Academic Editor: Eiji Tokunaga

Received: 6 February 2024
Revised: 22 February 2024
Accepted: 23 February 2024
Published: 26 February 2024

1. Introduction

In combustion engines, high-pressure fuel systems play a pivotal role in increasing efficiency and power. These systems operate in harsh conditions, subjecting their vital components to extreme forces, temperatures, and pressures. Achieving consistent and reliable performance is of utmost importance and demands efficient lubrication mechanisms that can combat wear and prevent potential failures. However, traditional lubrication methods face significant challenges when dealing with the unique dynamics of these systems. For diesel systems running on jet fuel and for increasing the pressures of gasoline injection systems, the relatively low viscosity of the fuels limits the effectiveness of conventional

lubrication pathways. This limitation leads to increased wear rates, particularly in the realm of reciprocating contacts within the fuel system, especially over extended periods, as recent research has confirmed [1–4]. Scuffing failure is also expected in this context.

With the incorporation of coatings and fuel additives to improve lubrication, the vulnerability of sliding steel surfaces to wear and degradation remains a persistent concern, as documented in numerous studies [4–11]. Many fuel pumps are fabricated from AISI 52100 tool steel or similar alloys, which is renowned for its impressive strength and wear resistance [3,12–16]. The gradual shift towards low-viscosity fuels like ethanol and gasoline-ethanol blends has further complicated matters. 52100 steel, while highly regarded for its wear resistance, exhibits higher wear rates and an increased susceptibility to scuffing failure when exposed to these alternative fuels [3]. This dilemma necessitates a re-evaluation of its reliability in fuel delivery systems. To navigate this challenge, it becomes important to explore innovative strategies for material enhancement, aligning our efforts with the contemporary sustainability goals that call for fuel systems that are both robust and eco-friendly.

This research endeavors to shed light on the tribological performance of steels with different alloying elements and hardness when subjected to two distinct counter-bodies (alumina and 52100 steel) in two chemically different low-viscosity fuel environments, providing valuable insights for addressing the pressing challenges faced by high-pressure fuel systems in modern combustion engines.

2. Materials and Experimental Procedures

2.1. Materials

In this study, we analyzed three different types of steels: 52100, CF2, and D2, each with its unique composition (Table 1). CF2 is made up of a mix of copper, nickel, and manganese [17,18], while D2 steel has extra chromium for added corrosion resistance but very little nickel and copper. We also included 52100 steel as reference steel because it is commonly used in pumps and bearings and has well-established properties. The roughness of all the flat samples and counterbodies was below 200 nm. This reference steel helped us compare and understand how these different steel samples performed. Our main goal was to understand how the unique compositions of the various alloying elements in each steel contribute to their tribological properties and performance such as wear behavior.

Table 1. Steel composition.

Steel	Fe wt.%	C wt.%	Cr wt.%	Mn wt.%	S wt.%	Si wt.%	P wt.%	Co wt.%	Mo wt.%	V wt.%	Ni wt.%	Cu wt.%
52100	Bal	1.1	1.6	0.45	0.025	0.30	0.025	-	-	-	-	-
CF2	Bal	0.06	-	0.52	-	-	-	-	-	-	2.58	2.48
D2	Bal	1.3	12	0.6	0.03	0.6	0.03	1	0.8	1.10	0.3	0.03

For this purpose, we studied these steels at two Vickers hardness levels, around 360 and 800. We heat-treated some of the steels and measured the hardness with the average of several indentations using a Buehler Wilson VH1102 Vickers indenter (Buehler, Lake Bluff, IL, USA). The hardness results are given in Table 2. Soft 52100 steel started with a hardness of 373 HV0.5 but was increased to 810 HV0.5 through a specific heat treatment process. CF2 steel had a measured hardness of 355 HV0.5 and was not hardened further. Soft D2 steel had a hardness of 371 HV0.5, which was increased to 787 HV0.5 after heat treatment.

Table 2. Average hardness of different steel.

Steels	Average Hardness (HV0.5)
Soft 52100	373 ± 15
Hard 52100	810 ± 14
Soft CF2	355 ± 10
Soft D2	371 ± 12
Hard D2	787 ± 15

2.2. Tribological Testing

Tribological tests were conducted in two different fuels, ethanol and decane, using a Phoenix TE-77 tribometer (Phoenix Tribology Ltd., Hampshire, UK). The effect of a chemically inert counterbody was investigated by comparing the tribological behavior of steels in contact with a 10 mm AISI 52100 ball and a 10 mm Al_2O_3 ball with roughness below 200 nm with both ethanol and decane as lubricants.

The reciprocating tribometer is a widely utilized instrument for studying the friction and wear behavior of materials under realistic operating conditions as shown in schematics in Figure 1. It provides precise control over testing parameters and enables accurate measurement of wear rates. Table 3 contains detailed information regarding the specific testing parameters used in this study. During the test, each steel sample was subjected to reciprocating sliding motion against the selected counterbody material, with the solvent environment serving as the lubricating medium. The solvents were continuously replenished to ensure full submersion of the samples for the whole duration of the tests. Each test was repeated at least 3 times.

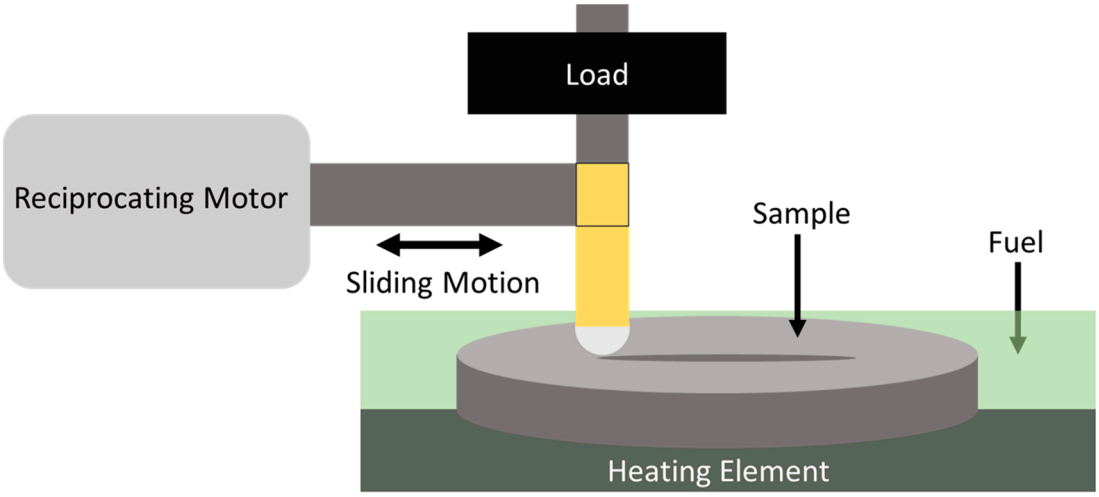

Figure 1. Schematic illustration showing reciprocating ball-on-disk sliding experiments in a fuel environment.

Table 3. Tribological testing parameters in fuel environments.

Operating Parameter	Value
Applied Load	10 N
Maximum Contact Pressure	1.01–1.18 GPa
Stroke Length	10 mm
Temperature	40 °C
Frequency	20 Hz
Average Sliding Velocity	400 mm/s

To determine the specific wear rate, the material loss of each sample after testing was measured and normalized by considering the sliding distance L and applied load W:

$$Wear\ rate = \frac{wear\ volume}{L\ W} \quad (1)$$

This normalization allowed for a direct comparison of the wear rates among different samples and under varying test conditions. Ethanol provided a polar alcohol environment similar to E-85, and decane provided an alkane environment similar to the main components of gasoline and kerosene jet fuels. Additionally, comparing the wear behavior with different counterbody materials, hardened AISI 52100 steel and Al_2O_3, provided insights into the tribological compatibility and wear mechanisms of the steels.

2.3. Wear Characterization

To analyze the wear tracks on the flat sides and the ball wear scars formed after the tribological tests, a standard Zeiss optical microscope was utilized. After the completion of the tribological testing, wear volumes were obtained from profilometry scans taken with a Filmetrics Profilm 3D profilometer (KLA Instruments, Milpitas, CA, USA). The wear volume of the entire wear track was obtained, allowing for the calculation of the wear rate for each set of testing conditions. Additionally, the wear volumes of the counterbody materials were determined using laser confocal measurements taken with a Zeiss Confocal Optical Microscope (Zeiss Microscope Central, Jena, Germany). The wear scar diameter was measured by averaging the major and minor axes and utilized to calculate the average wear volume of each counterbody.

Analysis of the chemical modifications inside the weartracks was performed using an FEI Nova 200 NanoLab scanning electron microscope (FEI, Hillsboro, OR, USA) equipped with an energy-dispersive X-ray spectroscope (EDS). Raman spectroscopy was performed using a Renishaw Confocal Raman Spectrometer (Renishaw, Dundee, IL, USA) (equipped with a 532 nm laser operating at 10% power, and the data acquisition was conducted over two seconds. The power density employed was sufficiently low to mitigate any potential artifacts arising from the laser beam. Raman spectroscopy was conducted to investigate the tribocatalytic behaviors of the steels—hard 52100, soft 52100, soft CF2, soft D2, and hard D2—after the reciprocating sliding tests within a decane environment against an alumina counterbody. By employing the results from optical microscopy and profilometry, a comprehensive characterization of the wear features of these steels was achieved.

2.4. Lubrication Analysis

To understand the lubrication status and degree of asperity interaction of the tribo-pair during the reciprocating motion in the tests, transient elastohydrodynamic lubrication (EHL) analyses were conducted with a mixed EHL model including a mass-conservation algorithm. This mixed EHL model and its numerical schemes were developed based on previous studies [19–29] with an efficient procedure for contact elasticity [29–33]. With the x-axis pointing along the moving direction and the y-axis the lateral direction, pressure distribution p between the tribo-pair is governed by the Reynolds equation:

$$\frac{\partial}{\partial x}\left(\frac{\rho h^3}{12\eta}\frac{\partial p}{\partial x}\right) + \frac{\partial}{\partial y}\left(\frac{\rho h^3}{12\eta}\frac{\partial p}{\partial y}\right) = \frac{u_1}{2}\frac{\partial(\theta\rho h)}{\partial x} + \frac{\partial(\theta\rho h)}{\partial t} \quad (2)$$

where h, ρ, and η are the geometric gap between the two surfaces, lubricant density, and viscosity, respectively. In the tests, the disk was stationary, while the velocity of the ball, u_1, was a sinusoidal function with a maximum speed of 0.628 m/s in the middle of the stroke. θ is the fractional film content [19], i.e., the ratio between the accumulated thickness occupied by the lubricant and the gap at that location. Gap $h(x,\ y,\ t)$ includes the combined surface

elastic deformation, $v(x,\ y,\ t)$, of the two surfaces, the spherical geometry at the vicinity of the contact, $\frac{x^2+y^2}{2R}$, and the initial separation at the center of the EHL zone, h_0.

$$h(x,\ y,\ t) = h_0(t) + \frac{x^2+y^2}{2R} + v(x,\ y,\ t) \tag{3}$$

Surface was not considered for simplicity. The density, ρ, and viscosity, η, of ethanol were modeled based on the work reported in [34] at different pressures and temperatures. However, experimental data for high pressure (beyond 200 MPa) were not available; therefore, values were extrapolated outside the low-pressure range using models as follows. Tabulated data at 40 °C degrees were provided by Prof. Assael based on formulae in [34] in a private communication. The variation of lubricant density ρ with pressure p was curve-fit with the Dowson–Higginson relationship:

$$\rho = 772.1\left(1 + \frac{1.01 \times 10^{-9}p}{1 + 2.16 \times 10^{-9}p}\right) \tag{4}$$

in the unit of kg/m^3. The viscosity data were curve-fitted with the same relationship in the unit of Pa.s:

$$\eta = 8.195 \times 10^{-4}\left(1 + \frac{5.61 \times 10^{-9}p}{1 + 0.402 \times 10^{-9}p}\right) \tag{5}$$

On the other hand, the pressure–viscosity coefficient of 5.08 GPa^{-1} was obtained for ethanol with the exponential viscosity model [35] from data up to 0.1 GPa, and it was used in the Hamrock–Dowson equation to find initial values of the central film thickness in the numerical simulations.

The properties of decane at different temperatures for pressure up to 89 MPa can be obtained from the Webbook of NIST (https://webbook.nist.gov/chemistry/fluid/, accessed on 22 February 2024). Under four different temperatures, Caudwell et al. [36] reported data including higher pressure situations and presented the following curve-fitted equations. The density of decane is:

$$\frac{\rho}{\rho_0} = \left(1 - 0.207\log_{10}\frac{10^{-6}p + B}{0.1 + B}\right)^{-1} \tag{6}$$

in the unit of kg/m^3 with pressure in Pa.

In Equation (6), ρ_0 is the density at ambient pressure, 0.1 MPa, which is a function of temperature T in K:

$$\rho_0 = 918.45 - 0.52524T - 3.949 \times 10^{-4}T^2 \tag{7}$$

and constant B is also a function of temperature T in K:

$$B = 398.06 - 1.49775T + 1.488 \times 10^{-3}T^2 \tag{8}$$

The viscosity of decane is:

$$\eta = \eta_0\left(\frac{10^{-6}p + E}{0.1 + E}\right)^D \tag{9}$$

in the unit of Pa.s. Here, η_0 is the viscosity at ambient pressure, 0.1 MPa:

$$\eta_0 = 1.7 \times 10^{-5}\exp\left(\frac{1045.98}{T - 30.80}\right) \text{ Pa.s} \tag{10}$$

and constants D and E are functions of temperature T in K, with:

$$D = 11.6438 - \frac{8608.68}{T} + \frac{1.79954 \times 10^6}{T^2} \quad (11)$$

and

$$E = 2670.84 - 12.8767T + 0.0162362T^2 \quad (12)$$

Likewise, using the data up to 0.1 GPa, the pressure-viscosity coefficient of 9.64 GPa^{-1} was obtained for decane with the exponential viscosity model.

The applied load, W, of 10 N should be balanced with the integrated pressure $p(x, y, t)$ over the interaction area:

$$W = \iint_{\Omega} p(x, y, t) dxdy \quad (13)$$

A series of meshes, with the same mesh numbers in both x and y directions, and the progress mesh densification (PMD) technique [24] were used to reduce computation time and achieve a high numerical accuracy. The coarsest mesh was 65 by 65, and the finest mesh was 513 by 513. The first-order backward scheme was used for the right-hand side terms of Equation (2). One-quarter of a reciprocating cycle was simulated, starting from the center location to the end of a stroke.

3. Results and Discussion

3.1. Lubrication Status Analyses

The density and viscosity curves of ethanol and decane at 40 °C were obtained from Equations (5) and (6), plotted in Figure 2.

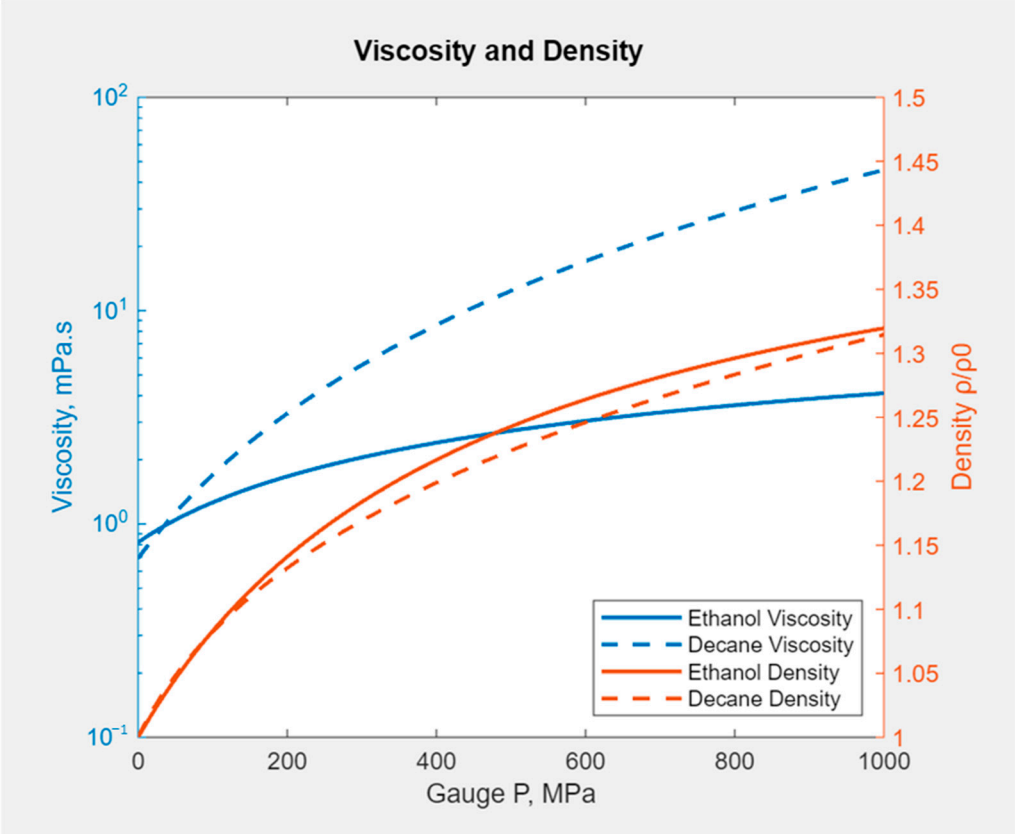

Figure 2. Comparison of properties for ethanol and decane at 40 °C.

Figure 3 shows the central and minimum film thickness values for the tests using ethanol as the lubricants, with steel or alumina balls of 10 mm diameter, at different times

within one sliding cycle normalized by the period. The results indicate that film thickness is only a few nanometers, which confirms that tribological testing with ethanol as a lubricant was in the boundary lubrication regime. Interestingly, the use of a steel ball results in the formation of a slightly thicker film than in the case of an alumina ball. It should be mentioned that in such thin gaps of a few nanometers, the lubricant molecules may behave differently from bulk. Therefore, these analyses should be interpreted qualitatively.

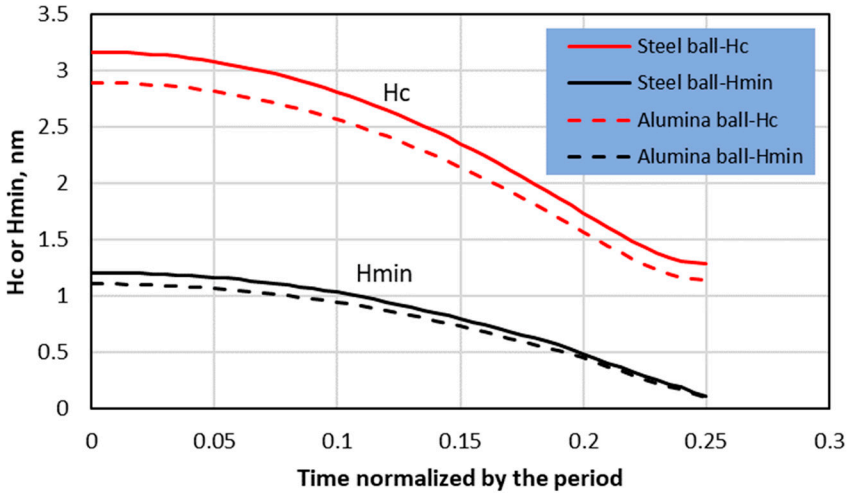

Figure 3. Central and minimum film thickness values for tests using steel and alumina balls, 10 mm in diameter, reciprocating motion with a maximum speed of 0.628 m/s and a normal load of 10 N. The lubricant is ethanol. Hc means central film thickness and Hmin minimum film thickness.

Figure 4 shows the central and minimum film thickness values at different times within one sliding cycle, normalized by the period, for the steel and alumina balls, using decane as the lubricant. Decane shows a slightly better film formation capability than ethanol, but these two fuels have similar trends change in film thickness during the test duration. With the film thickness in the range of several nanometers, it is fair to say that all the tribological tests were conducted in the boundary lubrication regime.

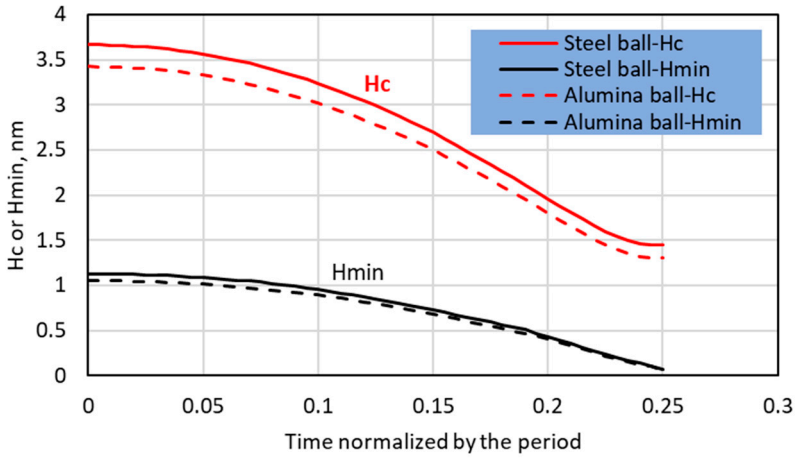

Figure 4. Central and minimum film thickness values for tests using steel and alumina ball, reciprocating motion with a maximum speed of 0.628 m/s and a normal load of 10 N. The lubricant is decane. Hc means central film thickness and Hmin minimum film thickness.

3.2. Friction and Wear Performance

The friction and wear of the steels were tested under boundary lubrication conditions in ethanol and decane. One representative test result of friction variation and microscope

image of surface wear are shown for each of the two different counterbodies, alumina and 52100, with ethanol lubrication in Figure 5. In Figure 5a, we compare the coefficient of friction of the soft and hard steels against the alumina counterbody with ethanol. The softer and harder steels had comparable friction behavior. In Figure 5c, when we used 52100 as the counterbody material, the coefficient of friction of the various materials varied over a greater range. Soft and hard 52100 had generally the lowest and highest values, while hard D2 dropped to a lower value towards the end of the test. Figure 5b,d show the worn surfaces of both the flat specimens and the counterbody balls. When we used alumina as the other material (Figure 5b), the width of the wear scar was less on both the ball and the flat surface.

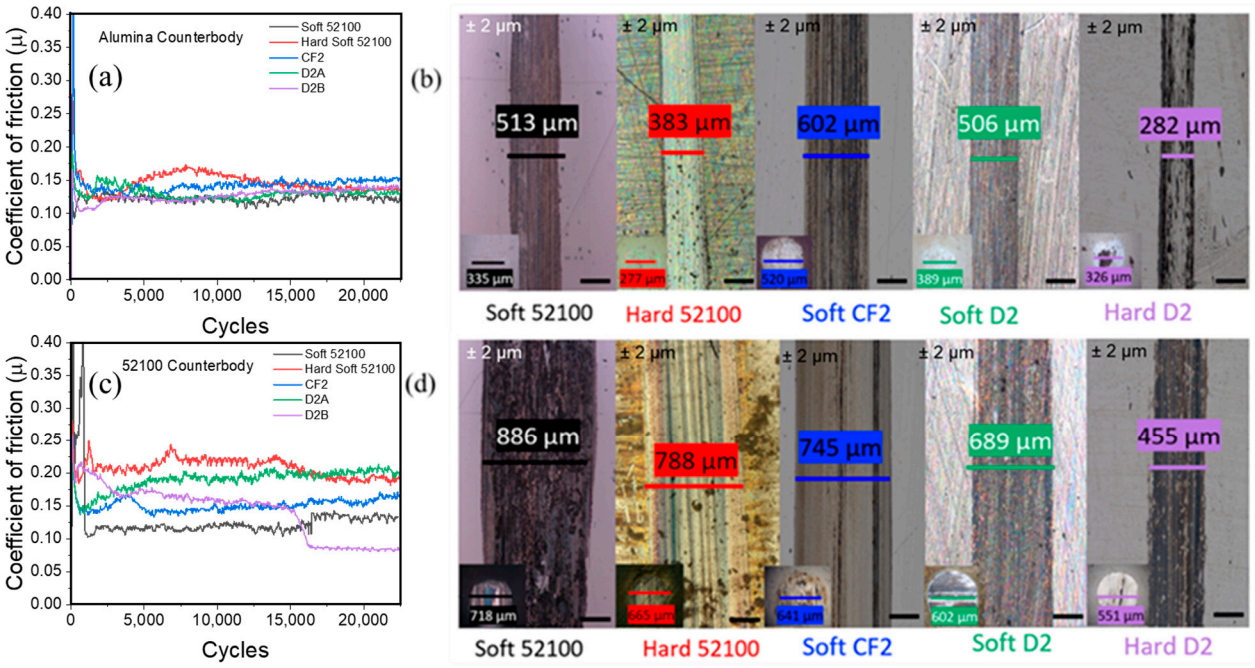

Figure 5. (**a**,**c**) Coefficient of friction behavior of soft and hard 52100, soft CF2, and soft and hard D2 steel against (**a**) Alumina counterbody (**c**) 52100 counterbody under high-frequency reciprocating at the frequency of 20 Hz under 10 N as a function of cycles in ethanol environment. (**b**,**d**) Surface morphology of wear tracks and counterface ball surfaces. The scale bar is 200 μm.

Representative coefficient of friction and optical microscope wear results for the hard and soft steels with the two counterbodies using decane as a lubricant are given in Figure 6. Figure 6a reveals the coefficient of friction in the decane environment with the alumina counterbody. Soft D2, hard D2, and soft 52100 had steady coefficients of friction which were also the lowest, while soft CF2 and hard 52100 had higher and more variable coefficients of friction throughout. Figure 6c illustrates a different result when 52100 was used as the counterbody material. As with ethanol lubrication, the 52100 counterbody resulted in a larger range of coefficients of friction. Hard D2 had the lowest coefficient of friction, with soft 52100 and soft CF2 slightly higher but close in value. Figure 6b,d show the wear track on both the flat and counterbody surfaces. The wear tracks caused by alumina as the counterbody material (Figure 6b) are visibly smaller on both the surfaces of the ball and the flat samples than those from the 52100 counterbody (Figure 6d).

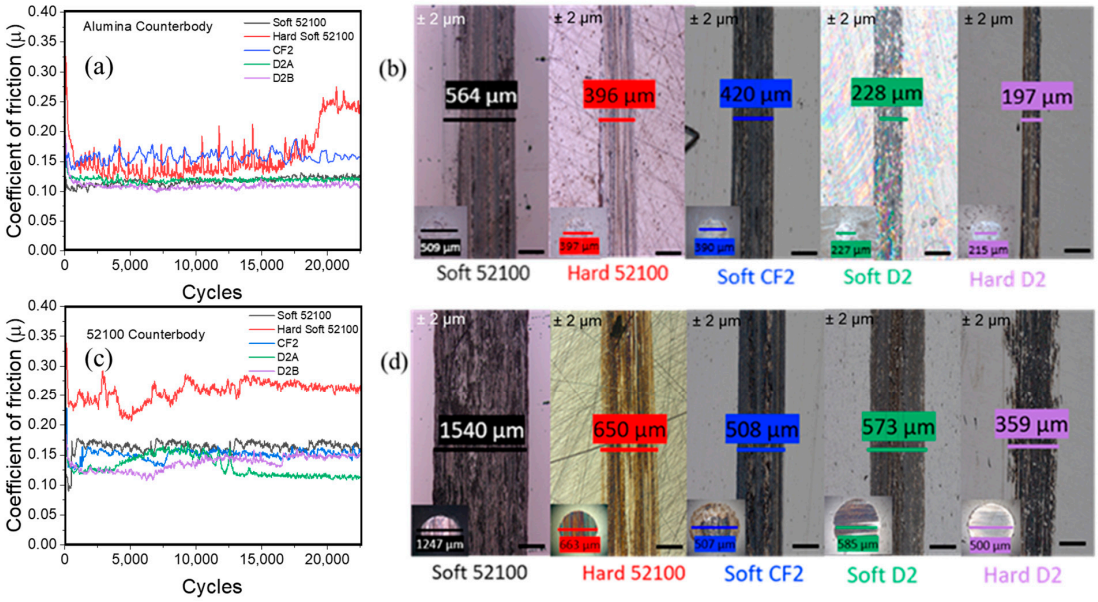

Figure 6. (**a**,**c**) Coefficient of friction behavior showing the performance of soft and hard 52100, soft CF2, and soft and hard D2 steel against (**a**) Alumina counterbody (**c**) 52100 counterbody under high-frequency reciprocating at the frequency of 20 Hz under 10 N as a function of cycles in decane environment. (**b**,**d**) Surface morphology of sliding paths and counterface ball surfaces. The scale bar is 200 μm.

We analyzed the steels (52100, CF2, and D2) by examining the average coefficients of friction, wear rate of the ball and the flat samples from three tests conducted in two fuel environments, and the wear profile from the tribology tests in ethanol and decane environments using both alumina and 52100 counterbody materials. The results are plotted in Figures 7 and 8.

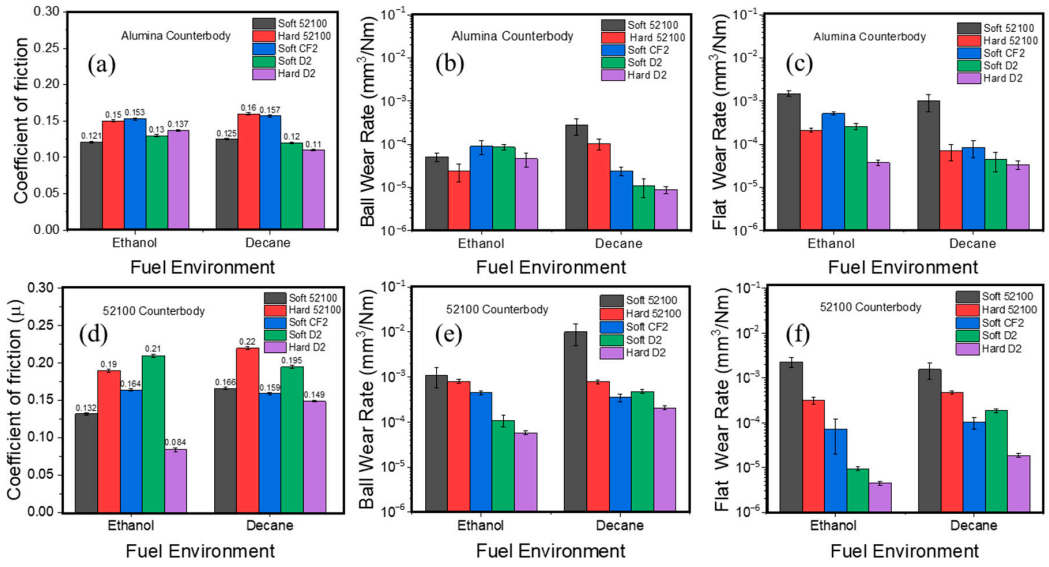

Figure 7. Summary of steady state friction values of soft and hard 52100, soft CF2, and soft and hard D2 steel (**a**) alumina counterbody and (**d**) 52100 counterbody under high-frequency reciprocating at a frequency of 20 Hz under 10 N load in ethanol and decane environment. Counter-body (ball) wear rate ((**b**) alumina counterbody & (**e**) 52100 counterbody) after sliding the same cycles against soft and hard 52100, soft CF2, and soft and hard D2 steel under ethanol and decane. The flat wear rate of soft and hard 52100, soft CF2, and soft and hard D2 steel against (**c**) alumina counterbody (**f**) 52100 counterbody under ethanol and decane environment.

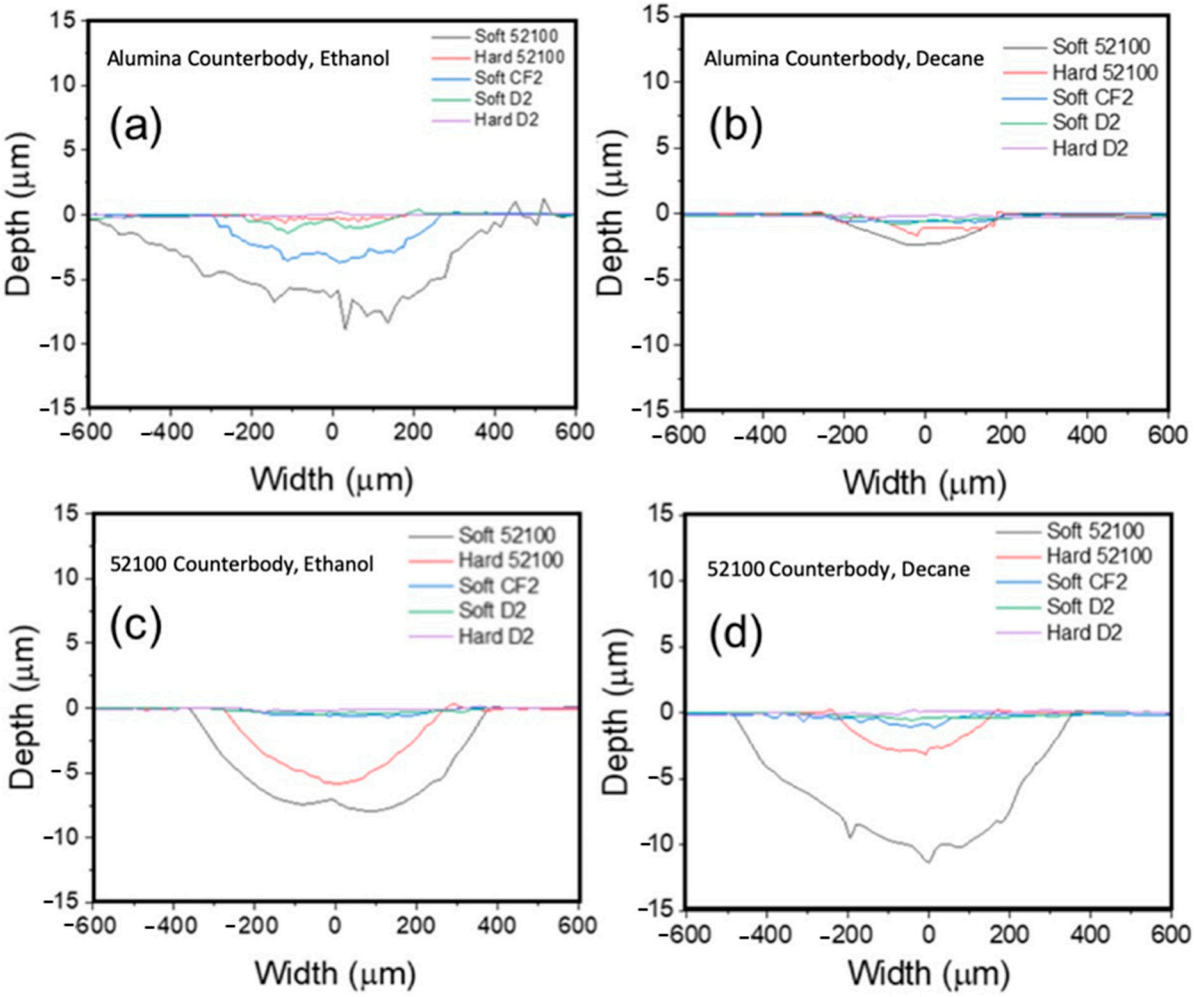

Figure 8. Surface profiles of soft and hard 52100, soft CF2 steel, soft and hard D2 ((**a**,**b**) alumina counterbody after sliding in ethanol and decane environment. Surface profiles of soft and hard 52100, soft CF2 steel, soft and hard D2 ((**c**,**d**) 52100 counterbody), after sliding in the ethanol and decane environment.

Figure 7a shows how the steel samples behaved in terms of friction when they were paired with alumina as the counterbody material. Notably, in the ethanol environment, soft 52100, soft CF2, and hard D2 displayed lower coefficients of friction. These three steels also had lower coefficients of friction in the decane environment, with hard D2 exhibiting the lowest compared to the other steel alloys.

The ball wear rates of the alumina counterbody are given in Figure 7b. In ethanol, it is evident that hard 52100 showed the lowest wear rate, followed by hard D2. In the decane environment, hard D2 stood out with the lowest wear rate of the ball, followed by soft D2.

Figure 7c plots the wear rate of flat steels when paired with an alumina counterbody. Remarkably, hard D2 exhibited the lowest flat-sample wear rate in both ethanol and decane environments, which can also be confirmed by the profilometry results shown in Figure 8a,d.

When we investigate how these materials performed in terms of friction against the 52100 counterbody material, as shown in Figure 7d, in both the ethanol or decane environment, hard D2 exhibited a lower coefficient of friction than the other steel samples. The ball wear rate (Figure 7e) and flat wear rate (Figure 7f) results demonstrated that hard D2 consistently displayed the lowest wear rate of both the steel itself and the counterbody. This trend observed for the ball and flat wear rates is consistent through the tests, even though the COF shows greater variability in values. The profilometry results

(Figure 8b,d) also revealed that hard D2 exhibits less material removal, compared to the other steel samples.

3.3. Characterization of the Wear Tracks

Since the tribological tests were performed in the boundary lubrication regime, the interactions of the solid surfaces should be responsible for the observed differences in the tribological behaviors. Characterization of the wear tracks was performed to understand the tribochemical effects at the sliding interfaces (Figure 9). The Raman spectra indicated the presence of characteristic carbon D and G bands, at approximately 1350 cm^{-1} and 1580 cm^{-1}, respectively. These Raman signatures have frequently been associated with the formation of carbon-based tribofilms [37–45].

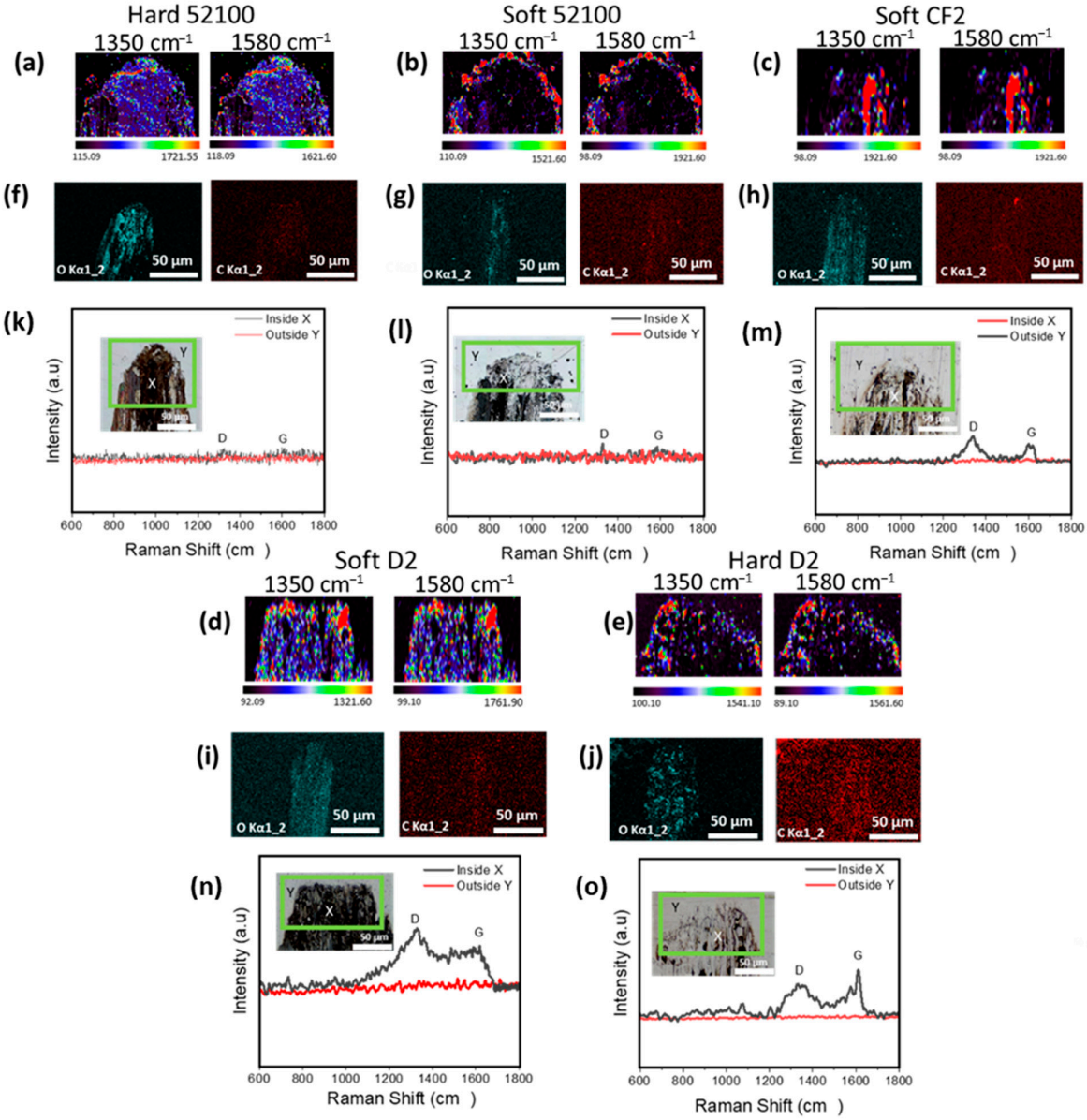

Figure 9. (**a**–**e**) Raman 2D maps for G and D peaks (1 µm lateral resolution) of hard 52100, soft 52100, soft CF2, soft D2 and hard D2 steel wear track in decane against alumina counterbody, (**f**–**j**) EDS maps of hard 52100, soft 52100, soft CF2, soft D2 and hard D2 steel wear track in decane against alumina counterbody, (**k**–**o**) Raman spectra inside the wear track of hard 52100, soft 52100, soft CF2, soft D2 and hard D2 steel wear track in decane against alumina counterbody.

The acquired series of Raman maps, spectra, and energy-dispersive x-ray spectroscopy (EDS) maps demonstrated the formation of carbon films during the sliding process. The hard and soft variants of 52100 steel displayed significantly weaker D and G signals when compared with CF2 and D2 steels. The Raman spectra of both soft CF2 and both hard and soft D2 steels exhibited stronger D and G signals, indicating a more efficient formation of the carbon films in these materials. This observation suggests that the steel composition is responsible for the formation of the protective carbon film which plays a critical role in further wear reduction [46]. Prior studies demonstrated that the presence of catalytic elements, such as Cu, Ni, Mo, etc., activate tribocatalytic processes [10,39,40]. In this case, the Cu, Ni, Cr, Mo, and V may have contributed to the tribocatalytic formation of the observed carbon films. Importantly, more efficient formation of the tribofilms also correlates with the improved wear resistance of these steels and the alumina counterbody observed in Figure 7b,c. The low wear of the hard 52100 in decane with alumina may be due to the higher amount of oxide observed in the EDS map of Figure 9f The formation of oxides was identified as a contributing factor in the wear behavior of the steels.

Raman spectra of soft variants of the CF2 and D2 steels displayed a higher intensity of the D band in comparison to that of the G band, indicating a higher level of disorder or structural imperfections within the formed carbon tribofilms [10,39–41]. Among these steels, the CF2 steel shows more distinguished peaks, suggesting a more ordered and graphitic-like structure, underlining more complete dissociation of hydrocarbon molecules and prevalence of carbon-carbon bonds which is in line with prior reports on carbon film formation on the surface of Cu clusters [39]. Meanwhile, though D2 steel also shows characteristic carbon peaks, the presence of additional peaks between the D and G bands suggests incomplete dissociation of C–H and C–O bonds and a rather tribopolymer-like structure of the formed film [10,40].

The current investigation suggests that chromium (Cr) and copper/nickel (Cu/Ni) are influential elements in D2 and CF2 steels, respectively. For instance, Cr_2O_3, a well-known catalyst, is responsible for producing a significant portion of the world's polyethylene, and D2 steel, with its 11.5 wt.% Cr content, demonstrates higher catalytic potential compared to 52100 steel with only 1.45 wt.% Cr. Similarly, Cu/Ni acts as a catalyst for alkane dehydrogenation.

Prior studies indicated that Cr_2O_3 is able to catalyze the formation of oligomers/polymers from polyalphaolefin and dodecane [43]. Given that the tribotesting was conducted in the air, the formation of Cr_2O_3 from Cr in D2 during testing aligns with these findings. Recent studies on chromizing steels [44] provide additional evidence supporting the positive effects of chromium on wear. The varying wear performance observed in ethanol and decane environments may be linked to the diverse catalytic activities of different elements toward these lubricants.

4. Conclusions

This study investigated the friction and wear behaviors of several steels when exposed to different lubrication environments and counterbody materials. Two types of fuel, ethanol and decane, two distinct counterbody materials, alumina and 52100 steel, and two hardness values were used to investigate how they influenced the tribological performance of the steels. The elastohydrodynamic analysis evaluated the changes in the film thickness during the initial test duration, revealing a modest dependence of film thickness on the counterbody material and the fuel chemistry, and confirmed that all tests were conducted in the boundary lubrication regime.

The results revealed that the tribological behavior trends were similar for alumina and 52100 steel counterbodies across different environments. Even though soft 52100 steel demonstrated low friction, its wear was the largest for both tested environments and counterface materials. Among all the tested materials, hard D2 steel experienced the lowest wear. 52100 and D2 steels showed opposite friction behavior when comparing hard and soft steels, with lower friction observed for softer 52100 and harder D2 steels. Meanwhile,

the wear of both flat and ball counterfaces was lower for harder candidates than for softer ones independent of the environment and counterbody.

Results from the Raman characterization suggested that alloying elements played a crucial role in determining the wear characteristics of the steels under investigation. Raman analysis revealed the presence of characteristic D and G bands in the Raman spectra collected from the wear tracks, suggesting the formation of carbon-based tribofilms contributing to additional protection of surfaces during sliding. Interestingly, softer variants of CF2 and D2 steels exhibited a higher D band intensity compared to that of the G band, indicating increased disorder or structural imperfections. Contrarily, the harder D2 steel showcased a stronger G band, indicative of a more ordered structure of carbon–carbon bonds. Furthermore, the role of alloying elements in the wear process was noteworthy. These elements appeared to impact the material's resistance to wear, suggesting that the specific composition of the alloys played a key role in determining the tribological performance. The results of the study highlight the significance of alloy composition as the primary factor influencing wear resistance. In support of this, literature studies indicate that specific elements play a crucial role in catalyzing the transformation of hydrocarbon molecules into polymers during rubbing.

These findings underscore the intricate relationship among steel alloy composition, structural properties (hardness), oxide formation, and the efficiency of carbon film formation during tribocatalytic processes, reflecting the wear performance of these steels. Through comprehensive evaluations of friction, wear, and surface topography, we highlight the importance of material compositions, counterbody materials, and environmental factors in defining the tribological performance of fuel-lubricated materials.

Author Contributions: Conceptualization, D.B., A.A.V., S.M.A. and S.P.B.; methodology, D.B., A.A.V., S.M.A.; experimental validation, A.Z.M., V.L.M., E.C. and M.E.; computational analysis, S.L. and Q.J.W.; resources, D.B., A.A.V., S.M.A., S.P.B., Y.-W.C. and Q.J.W.; data curation, A.Z.M., V.L.M., E.C., M.E., S.L., Q.J.W., S.P.B., S.M.A., A.A.V. and D.B.; writing—original draft preparation, A.Z.M., S.P.B., S.L. and D.B.; writing—review and editing, Y.-W.C., Q.J.W., S.M.A. and A.A.V.; supervision, D.B., S.M.A., A.A.V. and S.P.B. All authors have read and agreed to the published version of the manuscript.

Funding: This research was sponsored by the DEVCOM Army Research Laboratory and was accomplished under Cooperative Agreement Numbers W911NF-20-2-0198 and W911NF-21-2-0199. The views and conclusions contained in this document are those of the authors and should not be interpreted as representing the official policies, either expressed or implied, of the Army Research Laboratory or the U.S. Government. The U.S. Government is authorized to reproduce and distribute reprints for Government purposes notwithstanding any copyright notation herein.

Institutional Review Board Statement: Not applicable.

Informed Consent Statement: Not applicable.

Data Availability Statement: The authors confirm that the data supporting the findings of this study are available within the article.

Acknowledgments: This work was performed in part at the University of North Texas's (UNT) Materials Research Facility (MRF) and UNT's Advanced Materials and Manufacturing Processes Institute (AMMPI). The authors thank Vincent Hammond for assistance in obtaining specimens. The authors thank James Rodriguez for assistance with the measurements.

Conflicts of Interest: The authors declare that they have no known competing financial interests or personal relationships that could have appeared to influence the work reported in this manuscript.

References

1. Thiagarajan, D.; Vacca, A.; Watkins, S. On the lubrication performance of external gear pumps for aerospace fuel delivery applications. *Mech. Syst. Signal Process.* **2019**, *129*, 659–676. [CrossRef]
2. Cesur, I.; Ayhan, V.; Parlak, A.; Savaş, Ö.; Aydin, Z. The Effects of Different Fuels on Wear between Piston Ring and Cylinder. *Adv. Mech. Eng.* **2014**, *6*, 503212. [CrossRef]

3. Jacques, K.; Murthy, N.; Dixit, S.; Berman, D.; Berkebile, S. Method for tribological experiment to study scuffing initiation on AISI 52100 steel and hard ceramic coatings. *Tribol. Int.* **2021**, *160*, 107001. [CrossRef]
4. Lacey, P.I.; Westbrook, S.R. Fuel Lubricity Additive Evaluation *Interim Rep. BFLRF* 1997. Available online: https://apps.dtic.mil/sti/citations/ADA326098 (accessed on 12 January 2023).
5. Aird, R.T.; Forgham, S.L. The lubricating quality of aviation fuels. *Wear* **1971**, *18*, 361–380. [CrossRef]
6. Mitchell, K. *Continued Evaluation of Diesel Fuel Lubricity by Pump Rig Tests*; SAE Technical Paper; SAE International: Warrendale, PA, USA, 1998. [CrossRef]
7. Hsieh, P.Y.; Bruno, T.J. A perspective on the origin of lubricity in petroleum distillate motor fuels. *Fuel Process. Technol.* **2015**, *129*, 52–60. [CrossRef]
8. Jacques, K.; Joy, T.; Shirani, A.; Berman, D. Effect of Water Incorporation on the Lubrication Characteristics of Synthetic Oils. *Tribol. Lett.* **2019**, *67*, 105. [CrossRef]
9. Macknojia, A.; Ayyagari, A.; Zambrano, D.; Rosenkranz, A.; Shevchenko, E.V.; Berman, D. Macroscale Superlubricity Induced by MXene/MoS_2 Nanocomposites on Rough Steel Surfaces under High Contact Stresses. *ACS Nano* **2023**, *17*, 2421–2430. [CrossRef]
10. Shaha, K.; Pei, Y.; Martinez-Martinez, D.; De Hosson, J. Influence of hardness and roughness on the tribological performance of TiC/a-C nanocomposite coatings. *Surf. Coat. Technol.* **2010**, *205*, 2624–2632. [CrossRef]
11. Wang, L.; Gong, P.; Li, W.; Luo, T.; Cao, B. Mono-dispersed Ag/Graphene nanocomposite as lubricant additive to reduce friction and wear. *Tribol. Int.* **2020**, *146*, 106228. [CrossRef]
12. Wadumesthrige, K.; Ara, M.; Salley, S.O.; Ng, K.Y.S. Investigation of lubricity characteristics of biodiesel in petroleum and synthetic fuel. *Energy Fuels* **2009**, *23*, 2229–2234. [CrossRef]
13. Wu, X.; Cong, P.; Nanao, H.; Minami, I.; Mori, S. Tribological behaviors of 52100 steel in carbon dioxide atmosphere. *Tribol. Lett.* **2004**, *17*, 925–930. [CrossRef]
14. Türedi, E.; Yilmaz, M.; Senol, V. Tribological response of heat treated AISI 52100 steels against steel and ceramic counterparts. *Arch. Foundry Eng.* **2017**, *17*, 222–228. [CrossRef]
15. Elwasli, F.; Mzali, S.; Zemzemi, F.; Mkaddem, A.; Mezlini, S. Effects of initial surface topography and contact regimes on tribological behavior of AISI-52100/AA5083 materials' pair when reciprocating sliding. *Int. J. Mech. Sci.* **2018**, *137*, 271–283. [CrossRef]
16. Bosch, J.; DellaCorte, C. Rheological Characterization and Tribological Evaluation of Water-Based Lubricants in AISI 52100 Bearing Steel. *Tribol. Lett.* **2023**, *72*, 10. [CrossRef]
17. Ozimina, D.; Madej, M.; Styp-Rekowski, M. Antiwear additives as retarding agents of elements with ceramic coatings wear. *Ind. Lubr. Tribol.* **2010**, *62*, 275–278. [CrossRef]
18. Sun, H.; Li, D.; Diao, Y.; He, Y.; Yan, L.; Pang, X.; Gao, K. Nanoscale Cu particle evolution and its impact on the mechanical properties and strengthening mechanism in precipitation-hardening stainless steel. *Mater. Charact.* **2022**, *188*, 111885. [CrossRef]
19. Wijnant, Y.H. Contact Dynamics in the Field of Elastohydrodynamic Lubrication. 30 October 1998. Available online: https://research.utwente.nl/en/publications/contact-dynamics-in-the-field-of-elastohydrodynamic-lubrication (accessed on 15 January 2024).
20. Morales-Espejel, G.E.; Lugt, P.M.; Van Kuilenburg, J.; Tripp, J.H. Effects of surface micro-geometry on the pressures and internal stresses of pure rolling EHL contacts. *Tribol. Trans.* **2003**, *46*, 260–272. [CrossRef]
21. Qiu, M.; Lu, J.; Yin, Y. Numerical analysis of non-Newtonian TEHL line contact problem based on real-coded genetic algorithm. *Tribol. Int.* **2009**, *42*, 1052–1060. [CrossRef]
22. Chevalier, F.; Lubrecht, A.; Cann, P.; Colin, F. Film Thickness in Starved EHL Point Contacts. 1998. Available online: https://asmedigitalcollection.asme.org/tribology/article-abstract/120/1/126/439173 (accessed on 8 February 2024).
23. Wang, W.Z.; Li, S.; Shen, D.; Zhang, S.; Hu, Y.Z. A mixed lubrication model with consideration of starvation and interasperity cavitations. *Proc. Inst. Mech. Eng. Part J J. Eng. Tribol.* **2012**, *226*, 1023–1038. [CrossRef]
24. Pu, W.; Wang, J.; Zhu, D. Progressive Mesh Densification Method for Numerical Solution of Mixed Elastohydrodynamic Lubrication. *J. Tribol.* **2016**, *138*, 021502. [CrossRef]
25. Jiang, X.; Hua, D.Y.; Cheng, H.S.; Ai, X.; Lee, S.C. A Mixed Elastohydrodynamic Lubrication Model With Asperity Contact. *J. Tribol.* **1999**, *121*, 481–491. [CrossRef]
26. Nash, J. Continuity of Solutions of Parabolic and Elliptic Equations. 1958. Available online: https://www.jstor.org/stable/2372841 (accessed on 1 December 2023).
27. Lugt, P.M.; Morales-Espejel, G.E. A review of elasto-hydrodynamic lubrication theory. *Tribol. Trans.* **2011**, *54*, 470–496. [CrossRef]
28. Kubiak, K.; Mathia, T. Influence of roughness on contact interface in fretting under dry and boundary lubricated sliding regimes. *Wear* **2009**, *267*, 315–321. [CrossRef]
29. Wang, J.; Zhu, D. *Interfacial Mechanics: Theories and Methods for Contact and Lubrication*; CRC Press: Boca Raton, FL, USA, 2019; p. 636.
30. Stanley, H.M.; Kato, T. An FFT-Based Method for Rough Surface Contact. *J. Tribol.* **1997**, *119*, 481–485. [CrossRef]
31. Liu, S.; Wang, Q.; Liu, G. A versatile method of discrete convolution and FFT (DC-FFT) for contact analyses. *Wear* **2000**, *243*, 101–111. [CrossRef]
32. Peralta, A.; Kouris, D.; Knap, J.; Sieradzki, K. Eigenstrains and the elastic field of an adatom. *J. Mech. Phys. Solids* **1998**, *46*, 1557–1579. [CrossRef]

33. Ramesh, M.; Kailas, S.V.; Simha, K.R.Y. Micro and macro contact mechanics for interacting asperities. *Sadhana–Acad. Proc. Eng. Sci.* **2008**, *33*, 329–338. [CrossRef]
34. Sotiriadou, S.; Ntonti, E.; Velliadou, D.; Antoniadis, K.D.; Assael, M.J.; Huber, M.L. Reference Correlation for the Viscosity of Ethanol from the Triple Point to 620 K and Pressures up to 102 MPa. *Int. J. Thermophys.* **2023**, *44*, 40. [CrossRef]
35. Bair, S.; Liu, Y.; Wang, Q.J. The pressure-viscosity coefficient for newtonian ehl film thickness with general piezoviscous response. *J. Tribol.* **2006**, *128*, 624–631. [CrossRef]
36. Caudwell, D.R.; Trusler, J.P.M.; Vesovic, V.; Wakeham, W.A. Viscosity and density of five hydrocarbon liquids at pressures up to 200 MPa and temperatures up to 473 K. *J. Chem. Eng. Data* **2008**, *54*, 359–366. [CrossRef]
37. Grejtak, T.; Qu, J. Improving mechanical properties of carbon and tool steels via chromizing. *Adv. Appl. Ceram.* **2023**, *122*, 215–225. [CrossRef]
38. Meng, A.M.; Leech, H.L.-T. International, and Undefined 2019, Mechanical Properties and Tribological Behavior of Electroless Ni–P–Cu Coatings on Corrosion-Resistant Alloys under Ultrahigh Contact Stress with Sprayed. In *Tribology International*; Elsevier: Amsterdam, The Netherlands, 2019. Available online: https://www.sciencedirect.com/science/article/pii/S0301679X19303469 (accessed on 6 February 2024).
39. Pogrebnjak, A.D.; Bagdasaryan, A.A.; Pshyk, A.; Dyadyura, K. Adaptive multicomponent nanocomposite coatings in surface engineering. *Uspekhi Fiz. Nauk.* **2017**, *187*, 629–652. [CrossRef]
40. Jacques, K.; Shirani, A.; Smith, J.; Scharf, T.W.; Walck, S.D.; Berkebile, S.; Eryilmaz, O.L.; Voevodin, A.A.; Aouadi, S.; Berman, D. MoVN-Cu coatings for in situ tribocatalytic formation of carbon-rich tribofilms in low-viscosity fuels. *ACS Appl. Mater. Interfaces* **2023**, *15*, 30070–30082. [CrossRef] [PubMed]
41. Shirani, A.; Li, Y.; Smith, J.; Curry, J.; Lu, P.; Wilson, M.; Chandross, M.; Argibay, N.; Berman, D. Mechanochemically driven formation of protective carbon films from ethanol environment. *Mater. Today Chem.* **2022**, *26*, 101112. [CrossRef]
42. Berman, D.; Erdemir, A. Achieving Ultralow Friction and Wear by Tribocatalysis: Enabled by *In-Operando* Formation of Nanocarbon Films. *ACS Nano* **2021**, *15*, 18865–18879. [CrossRef] [PubMed]
43. Huynh, K.K.; Pham, S.T.; Tieu, K.A.; Wan, S. Tribocatalysis Induced Carbon-Based Tribofilms—An Emerging Tribological Approach for Sustainable Lubrications. *Lubricants* **2023**, *11*, 327. [CrossRef]
44. Fu, X.; Cao, L.; Wan, Y.; Li, R. Superlubricity achieved with TiN coatings via the in situ formation of a carbon-based film at the sliding interfaces. *Ceram. Int.* **2021**, *47*, 33917–33921. [CrossRef]
45. Fu, X.; Guo, S.; Wan, Y.; Zheng, C.; Li, Q.; Liu, B. Superlubricity of TiN coating using glycerol with the addition of Cu nanoparticles. *Tribol. Int.* **2023**, *181*, 108327. [CrossRef]
46. Ronkainen, H.; Likonen, J.; Koskinen, J.; Varjus, S. Effect of tribofilm formation on the tribological performance of hydrogenated carbon coatings. *Surf. Coat. Technol.* **1996**, *79*, 87–94. [CrossRef]